ChemComm

Enhancing Cu–ligand interaction for efficient CO_2 reduction towards multi-carbon products†

Jingyi Chen,‡[a] Lei Fan,‡[a] Yilin Zhao, [ID][a] Haozhou Yang, [ID][a] Di Wang,[a] Bihao Hu,[a] Shibo Xi[b] and Lei Wang [ID] *[ac]

Electrochemical CO_2 reduction (CO_2R) to valuable products provides a promising strategy to enable CO_2 utilization sustainably. Here, we report the strategy of using Cu-DAT (3,5-diamino-1,2,4-triazole) as a catalyst precursor for efficient CO_2 reduction, demonstrating over 80% selectivity towards multicarbon products at 400 mA cm^{-2}, with intrinsic activity over 19 times higher than that of Cu nanoparticles. The catalyst's active phase is determined to be metallic copper wrapped with the DAT ligand. We attribute this enhanced CO_2R performance to the accelerated steps of *CO adsorption and C–C coupling induced by the closely cooperated DAT ligand.

Electrochemical CO_2 reduction (CO_2R) has gained increasing attention as a promising approach to tackle the challenges of CO_2 emissions, owing to its ability of converting CO_2 into value-added chemicals when powered by renewable electricity.[1,2] Among numerous metal-based electrocatalysts,[3] Cu-based materials possess moderate intermediate CO binding strength, favouring the formation of multi-carbon (C_{2+}) products (*i.e.*, ethylene, ethanol).[4,5] Several strategies have been employed to further promote the formation of C_{2+} products, such as organic modification,[6–9] alloying[10,11] and introducing a dopant,[12,13] *etc.* Recently, gas diffusion electrode (GDE)[14,15] based CO_2R has largely alleviated the severe CO_2 diffusion limitations in conventional H-cells, enabling CO_2R at an industrially relevant current density.[16–19] However, a highly alkaline environment is typically necessary for achieving high selectivity towards C_{2+} products in GDE reactors.[20] Consequently, severe CO_2 loss,

carbonate salt formation and catalyst structural damage can occur, leading to impeded CO_2 diffusion and deteriorated activity.[21–23] In contrast, neutral electrolytes (*i.e.*, KHCO₃, KCl) can preserve the catalyst integrity and mitigate salt precipitation problems, allowing stable operation of CO_2R.[24] Herein, we demonstrate the optimization of the microenvironment for CO_2R in neutral electrolytes through the introduction of an amino group-rich ligand, resulting in substantially enhanced activity towards C_{2+} products.

We first conducted CO_2R measurements based on the physical mixture of commercial copper nanoparticles (CuNPs) and 3,5-diamino-1,2,4-triazole (DAT), a ligand rich in amino groups, in a typical flow cell in 1 M KHCO₃ (Fig. 1a). As shown in Fig. 1b and Fig. S1 (ESI†), the C_{2+} products selectivity increased significantly (*i.e.*, from <47% to >65%) as the DAT to CuNP ratio increases, indicating the profound promotion effect attributed to the DAT ligand. Notably, the overpotential at 300 mA cm^{-2} also decreased by as much as ~100 mV after the introduction of DAT, indicating the enhanced intrinsic activity towards C_{2+} products (all electrode potentials mentioned here are *vs.* RHE, unless otherwise defined). Energy-dispersive X-ray spectroscopy (EDS) (Fig. S2, ESI†) suggests the even dispersion of N and Cu elements after CO_2R, indicating that the ligand effect is originated from the intimate contact between the DAT ligand and the Cu active-sites. However, it is obvious that the interface between the DAT ligand and Cu particles is not optimized (Fig. S3, ESI†). Hence, to further promote the CO_2R performance, particularly the activity and selectivity towards C_{2+} products, we speculate that it would be beneficial to employ the Cu(ɪɪ)-DAT-based complex as a catalyst precursor for CO_2R, so that maximized contact between Cu active-sites and the DAT ligand can be achieved.

We then prepared an organometallic complex using Cu^{2+} (CuSO₄) as the metal center and DAT as the chelating ligand based on a modified procedure,[25] and the obtained complex is denoted as CuDAT (Fig. 1c).[26,27] Transmission electron microscopy (TEM) presents the morphology of the CuDAT particles (Fig. 1d), with a diameter of ~100 nm and lattice spacing of

[a] *Department of Chemical and Biomolecular Engineering, National University of Singapore, 4 Engineering Drive 4, 117585, Singapore.*
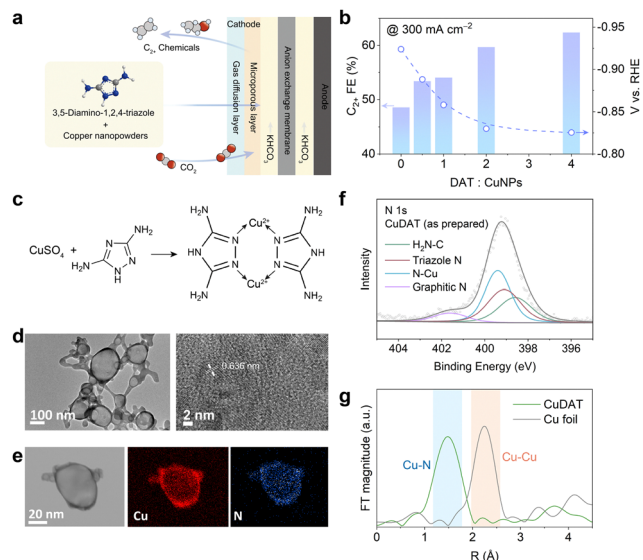*E-mail: wanglei8@nus.edu.sg*

[b] *Institute of Sustainability for Chemicals, Energy and Environment, A*STAR, 1 Pesek Road, Jurong Island, 627833, Singapore*

[c] *Centre for Hydrogen Innovations, National University of Singapore, 4 Engineering Drive 4, 117585, Singapore*

‡ Jingyi Chen and Lei Fan have contributed equally to this work.

Fig. 1 (a) Schematic of CO_2R in a flow cell using a physical mixture of CuNPs and DAT ligand. (b) C_{2+} selectivity and cathodic potential at 300 mA cm^{-2} with different ratios of DAT to CuNPs. Increasing ligand content leads to enhanced C_{2+} selectivity and reduced overpotential. (c) Synthetic approach and chemical structure of CuDAT. (d) TEM images, (e) EDS mapping and (f) N 1s XPS of the as-synthesized CuDAT. (g) Cu K edge FT-EXAFS of as-prepared CuDAT and Cu foil.

$\sim$0.636 nm. The crystallinity is further elucidated by XRD (Fig. S4, ESI†). Besides, the EDS mapping (Fig. 1e) confirms the uniform dispersion of Cu and N. X-ray photoelectron spectroscopy (XPS) suggests that the Cu centers remain as Cu^{2+}, with Cu $2p_{1/2}$ and $2p_{3/2}$ located at 953.6 eV and 934.6 eV, respectively (Fig. S5, ESI†).[28,29] Additionally, N species from the DAT ligand (–NH$_2$ and the triazole heterocycle) and the Cu–N bond can be clearly deconvoluted (Fig. 1f), in agreement with the proposed structure.[30,31] Moreover, Fourier transformation of the extended X-ray absorption fine structure (FT-EXAFS) consolidates the Cu–N bond around R = 1.5 Å (Fig. 1g),[32] suggesting the coordination between Cu^{2+} and DAT. The complex assembly is also manifested by attenuated total reflectance Fourier transform infrared spectroscopy (ATR-FTIR) (Fig. S6, ESI†), exhibiting the characteristic peaks of –NH$_2$ stretching at 3400 cm^{-1}, –NH stretching at 3300 cm^{-1}, –NH$_2$ bending at 1640 cm^{-1} and C–NH$_2$ stretching at 1050 cm^{-1}, in line with the characteristic signals of the DAT ligand.[33]

The CO_2R performance of CuDAT was assessed in a flow cell (Fig. 2). Notably, CuDAT exhibited high faradaic efficiency (FE) of >80% towards C_{2+} products at 400 mA cm^{-2}, which is comparable, if not higher, compared to the state-of-the-art CO_2R electrocatalysts under neutral conditions.[34] In contrast, CuNPs only delivered <60% FE (C_{2+}) under the same conditions (Fig. S7, ESI†). Additionally, CuDAT exhibited much lower overpotential compared to CuNPs at the same C_{2+} current density (Fig. 2b). To assess the intrinsic activity of CuDAT, we estimated the electrochemical active surface area (ECSA) of both CuDAT and CuNPs (Fig. S8, ESI†).[35] Strikingly, at a modest overpotential of −0.86 V $vs.$ RHE, the ECSA-normalized $j_{C_{2+}}$ of CuDAT is over 19 times higher than that of CuNPs (Fig. S9, ESI†).
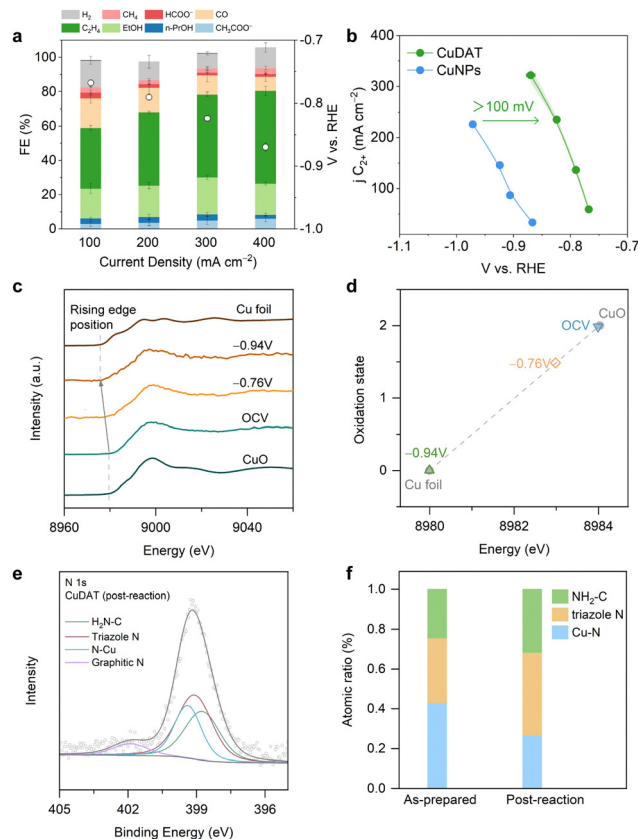
Fig. 2 (a) CO_2R performance on CuDAT in 1 M KHCO$_3$. (b) $j_{C_{2+}}$ on the function of the overpotential for CuDAT and CuNPs. (c) $Operando$ Cu K-edge XANES for CuDAT during CO_2R in a flow cell. (d) Oxidation state, deduced from the rising edge energy of Cu K edge XANES in CuDAT during CO_2R at different overpotentials. (e) N 1s XPS of the post-CO_2R CuDAT and (f) atomic percentage of N species for as prepared and post-reaction CuDAT. Triazole N and amino N were largely reserved.

Moreover, CuDAT also demonstrated promising CO_2R stability at 200 mA cm^{-2} (Fig. S10, ESI†). Overall, we demonstrate that applying an organometallic complex derived catalyst could be an effective strategy in enhancing the intrinsic activity and selectivity of Cu for C_{2+} products.

To explore the changes in the chemical state of Cu in CuDAT during CO_2R, we performed $operando$ X-ray absorption fine structure (XAFS) experiments using the same flow cell. As shown in Fig. 2c, the rising edge energy of the Cu K-edge X-ray absorption near edge structure (XANES) decreases gradually from open circuit voltage (OCV) to −0.94 V, reflecting the transition of oxidized Cu to its metallic state (Fig. 2d). This is further evidenced by the SEM and TEM images (Fig. S11, ESI†), in which drastic morphological changes occurred after CO_2R. Crucially, after CO_2R, the Cu (111) lattice is identified and forms aggregated particles $\sim$5 nm (Fig. S12, ESI†). Additionally, the post-reaction CuDAT sample exhibits a discernible Cu (111) peak on the XRD spectrum, providing further confirmation of the transition from Cu^{2+} to metallic Cu (Fig. S13, ESI†). The increased peak width is indicative of the small size of the Cu nanoparticles based on the Scherrer equation.[36] In comparison with the XRD pattern of as-prepared CuDAT, the original

crystallinity is disrupted, underscoring the structural reconstruction that occurs during CO_2R (Fig. S14, ESI†). Additionally, cross-section EDS mapping reveals the uniform dispersion of N and Cu elements, indicating that N-containing ligands are retained (Fig. S15, ESI†). Moreover, we found the existence of triazole N at 399.1 eV, amino N at 398.6 eV and N coordinated with Cu at 399.4 eV (Fig. 2e and f). Furthermore, FTIR spectra exhibit characteristic peaks of $-NH_2$ stretching at 3400 cm^{-1}, $-NH_2$ bending at 1640 cm^{-1}, and $C-NH_2$ stretching at 1050 cm^{-1} (Fig. S16, ESI†).[37] Taken together, we conclude that during CO_2R, the Cu centers were reduced and formed small Cu clusters/particles, while the DAT ligand remained intact and maintained intimate interaction with the Cu active sites.

In situ attenuated total reflection surface-enhanced infrared absorption spectroscopy (ATR-SEIRAS) was carried out to probe the reaction intermediates (Fig. 3a, Fig. S17, ESI†). Absorption bands located at ~ 2050 cm^{-1} were found corresponding to the $C\equiv O$ stretching mode of $*CO_L$ (linearly bonded CO).[38] After emerging at -0.5 V, the band intensity quickly decreases from -0.6 V to -1.1 V, indicating the rapid consumption of the $*CO$ intermediate due to the C–C coupling towards C_{2+} products. Moreover, the $*CO$ band position undergoes blue-shift first followed by red-shift along with the increase of overpotential,[39] which is caused by both the changes in $*CO$ coverage and the Stark shift effect.[40,41] Besides, the $*CO_L$ absorbance on CuNPs increases gradually from -0.5 V to -0.8 V (Fig. 3b). In contrast, $*CO_L$ on CuDAT shows a sharp increase and quickly reaches its maximum at -0.65 V, indicating the facilitated $*CO$ adsorption on CuDAT compared to that of CuNPs. Passing the $*CO_L$ absorbance maximum, CuDAT exhibits a more rapid decrease of the $*CO$ band intensity than CuNPs, suggesting the accelerated rate for producing multi-carbon products.[42,43] Moreover, the $*CO$ band on CuDAT appears at lower wavenumber, consolidating its favoured $*CO$ adsorption (Fig. 3c).[44]

The preferred $*CO$ adsorption is further confirmed through CO stripping experiments (Fig. S18, ESI†). In comparison to CuNPs, CuDAT displays a CO stripping peak at more positive overpotential, denoting a stronger $*CO$ adsorption on the Cu sites. To underscore the influence of the DAT ligand, we studied *in situ* ATR-SEIRAS on the physical mixture of CuNPs and DAT ligand as the catalyst composite during CO_2R (Fig. S19a, ESI†). Upon the introduction of the DAT ligand, the $*CO_L$ absorbance band undergoes more rapid emergence and decrease than that of CuNPs as the overpotential increases. This implies the acceleration of both $*CO_L$ adsorption and C–C coupling (Fig. S19b, ESI†). Additionally, the $*CO_L$ absorbance band undergoes a redshift with the ligand addition at -0.7 V, further confirming the favoured $*CO$ adsorption after the introduction of the DAT ligand (Fig. S19c, ESI†).

To conclude, we attribute the enhanced C_{2+} activity of CuDAT to the optimized binding strength of surface $*CO$, achieved through intimate Cu/ligand contact. This underscores the effectiveness of establishing such close interactions to maximize the promotion effect.

It is worthwhile to develop cost-effective approaches that can directly convert diluted CO_2 streams into valuable chemicals and fuels.[45,46] However, significant concentration overpotential is anticipated when using a low-concentration CO_2 stream, especially at high current densities. Nevertheless, we evaluated CuDAT for CO_2R using low-concentration CO_2 streams (Fig. 4a, b and Fig. S20, ESI†), as amino-functionalized materials have demonstrated prominent capabilities for local CO_2 enrichment.[47] At 300 mA cm^{-2}, it is encouraging to observe that CuDAT exhibits both higher CO_2R selectivity and significantly reduced overpotential compared to CuNPs across all CO_2 partial pressures (p_{CO_2}). Specifically, CuDAT maintains high CO_2R selectivity ($>80\%$) at 0.2 atm of CO_2 (Fig. 4c).
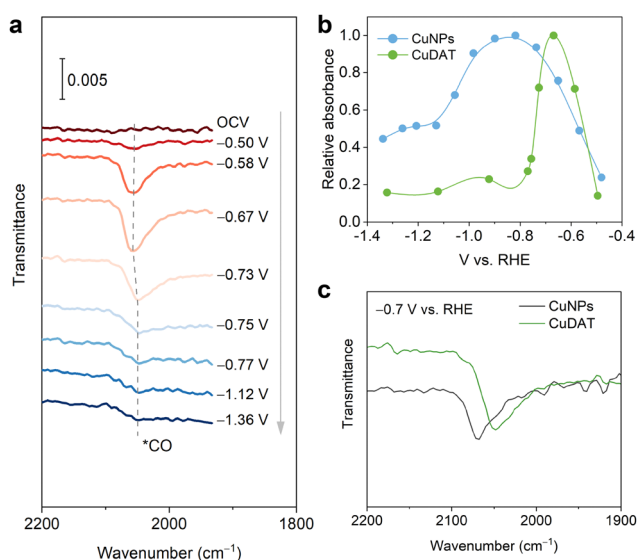

Fig. 3 (a) *In situ* ATR-SEIRAS of CuDAT. (b) Relative absorbance of the $*CO_L$ band for CuDAT and CuNPs. (c) $*CO_L$ band in *in situ* ATR-SEIRAS at -0.7 V *vs.* RHE.
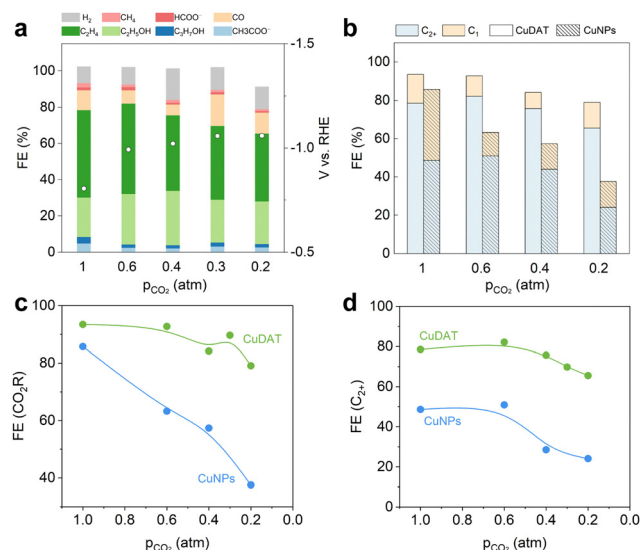

Fig. 4 (a) CO_2R on CuDAT with different CO_2 concentrations at 300 mA cm^{-2}. (b) CO_2R performance comparison between CuDAT and CuNPs. (c) CO_2R selectivity and (d) FE(C_{2+}) of CuDAT and CuNPs at different CO_2 partial pressures.

Additionally, compared with CuNPs, CuDAT shows reduced overpotential at 300 mA cm^{-2} by >30 mV at each p_{CO2} (Fig. S21, ESI†). Moreover, CuDAT maintains high C$_{2+}$ selectivity (over 70%) p_{CO_2} of 0.3 atm (Fig. 4d), significantly higher than those of CuNPs. These stark contrasts underscore the notable CO$_2$ enrichment capability of CuDAT. It is worth noting that the C$_{2+}$ formation during CO$_2$R initially increased and then began to decrease at p_{CO_2} around 0.4 atm for both catalysts (Fig. S22, ESI†). We attribute this phenomenon to potential-dependent changes in selectivity,[48] as the higher overpotentials (increased concentration overpotential) are favoured for C$_{2+}$ formation.

To summarize, we present a strategy to enhance CO$_2$R towards C$_{2+}$ products by constructing catalyst precursors through complexation of Cu with organic ligands possessing desirable properties. Owing to the intimate interactions between the Cu active sites and the organic ligands, CuDAT exhibits outstanding CO$_2$R performance towards C$_{2+}$ products. Based on detailed mechanistic investigations, the enhanced C$_{2+}$ production on CuDAT is attributed to the facilitated *CO adsorption and accelerated C–C coupling rate, induced by the closely cooperated DAT ligands. Moreover, CuDAT also demonstrates great potential for low-concentration CO$_2$ reduction.

Conflicts of interest

There are no conflicts to declare.

References

1 L. Fan, C. Xia, F. Yang, J. Wang, H. Wang and Y. Lu, *Sci. Adv.*, 2020, **6**, eaay3111.
2 D. Karapinar, C. E. Creissen, J. G. Rivera de la Cruz, M. W. Schreiber and M. Fontecave, *ACS Energy Lett.*, 2021, **6**, 694–706.
3 C. Yang, Y. Wang, L. Qian, A. M. Al-Enizi, L. Zhang and G. Zheng, *ACS Appl. Energy Mater.*, 2021, **4**, 1034–1044.
4 J. Chen and L. Wang, *Adv. Mater.*, 2022, **34**, e2103900.
5 A. Bagger, W. Ju, A. S. Varela, P. Strasser and J. Rossmeisl, *ACS Catal.*, 2019, **9**, 7894–7899.
6 Y. Zhao, X. Liu, J. Chen, J. Chen, J. Chen, L. Fan, H. Yang, S. Xi, L. Shen and L. Wang, *Proc. Natl. Acad. Sci. U. S. A.*, 2023, **120**, e2218040120.
7 Q. Zhu, C. J. Murphy and L. R. Baker, *J. Am. Chem. Soc.*, 2022, **144**, 2829–2840.
8 J. Chen, X. Liu, S. Xi, T. Zhang, Z. Liu, J. Chen, L. Shen, S. Kawi and L. Wang, *ACS Nano*, 2022, **16**, 13982–13991.
9 J. Chen, L. Chen, J. Chen, D. Wang, Y. Zhao, L. Wen, S. Xi and L. Wang, *Appl. Catal., B*, 2024, **343**, 123551.
10 Y. Qiao, G. Kastlunger, R. C. Davis, C. A. G. Rodriguez, A. Vishart, W. Deng, Q. Xu, S. Li, P. Benedek, J. Chen, J. Schröder, J. Perryman, D. U. Lee, T. F. Jaramillo, I. Chorkendorff and B. Seger, *ACS Catal.*, 2023, **13**, 9379–9391.
11 X. Chen, D. A. Henckel, U. O. Nwabara, Y. Li, A. I. Frenkel, T. T. Fister, P. J. A. Kenis and A. A. Gewirth, *ACS Catal.*, 2020, **10**, 672–682.
12 Y. Lan, G. Niu, F. Wang, D. Cui and Z. Hu, *ACS Appl. Mater. Interfaces*, 2020, **12**, 36128–36136.
13 C. Tang, Z. Chen, Y. Wang, T. Xiao, X. Li, C. Zheng, X. Xu and Z. Sun, *ACS Catal.*, 2022, **12**, 11838–11844.
14 B. Kim, F. Hillman, M. Ariyoshi, S. Fujikawa and P. J. A. Kenis, *J. Power Sources*, 2016, **312**, 192–198.
15 L. Chen, J. Chen, L. Fan, J. Chen, T. Zhang, J. Chen, S. Xi, B. Chen and L. Wang, *ACS Catal.*, 2023, **13**, 11934–11944.
16 T. Burdyny and W. A. Smith, *Energy Environ. Sci.*, 2019, **12**, 1442–1453.
17 M. F. Philips, D. Pavesi, T. Wissink, M. C. Figueiredo, G.-J. M. Gruter, M. T. M. Koper and K. J. P. Schouten, *ACS Appl. Energy Mater.*, 2022, **5**, 1720–1730.
18 Z.-Z. Niu, F.-Y. Gao, X.-L. Zhang, P.-P. Yang, R. Liu, L.-P. Chi, Z.-Z. Wu, S. Qin, X. Yu and M.-R. Gao, *J. Am. Chem. Soc.*, 2021, **143**, 8011–8021.
19 F. P. García de Arquer, C.-T. Dinh, A. Ozden, J. Wicks, C. McCallum, A. R. Kirmani, D.-H. Nam, C. Gabardo, A. Seifitokaldani, X. Wang, Y. C. Li, F. Li, J. Edwards, L. J. Richter, S. J. Thorpe, D. Sinton and E. H. Sargent, *Science*, 2020, **367**, 661–666.
20 Y. Zhao, X. Zu, R. Chen, X. Li, Y. Jiang, Z. Wang, S. Wang, Y. Wu, Y. Sun and Y. Xie, *J. Am. Chem. Soc.*, 2022, **144**, 10446–10454.
21 J. Gu, S. Liu, W. Ni, W. Ren, S. Haussener and X. Hu, *Nat. Catal.*, 2022, **5**, 268–276.
22 R. Lin, J. Guo, X. Li, P. Patel and A. Seifitokaldani, *Catalysts*, 2020, **10**, 473–507.
23 Y. Wu, L. Charlesworth, I. Maglaya, M. N. Idros, M. Li, T. Burdyny, G. Wang and T. E. Rufford, *ACS Energy Lett.*, 2022, **7**, 2884–2892.
24 X. Zhang, J. Li, Y. Y. Li, Y. Jung, Y. Kuang, G. Zhu, Y. Liang and H. Dai, *J. Am. Chem. Soc.*, 2021, **143**, 3245–3255.
25 F. R. Brushett, M. S. Thorum, N. S. Lioutas, M. S. Naughton, C. Tornow, H.-R. M. Jhong, A. A. Gewirth and P. J. A. Kenis, *J. Am. Chem. Soc.*, 2010, **132**, 12185–12187.
26 E. Aznar, S. Ferrer, J. Borrás, F. Lloret, M. Liu-González, H. Rodríguez-Prieto and S. García-Granda, *Eur. J. Inorg. Chem.*, 2006, 5115–5125.
27 S. Fonseca and L. M. C. Pinto, *ACS Omega*, 2020, **5**, 1581–1585.
28 L. Lu, X. Sun, J. Ma, D. Yang, H. Wu, B. Zhang, J. Zhang and B. Han, *Angew. Chem., Int. Ed.*, 2018, **57**, 14149–14153.
29 G. Iijima, H. Yamaguchi, T. Inomata, H. Yoto, M. Ito and H. Masuda, *ACS Catal.*, 2020, **10**, 15238–15249.
30 S. Mukherjee, M. Das, A. Manna, R. Krishna and S. Das, *J. Mater. Chem. A*, 2019, **7**, 1055–1068.
31 N. Zhao, Z. Shi, R. Chenitz, F. Girard and A. Mokrini, *Membranes*, 2020, **10**, 301.
32 D. Chen, L. H. Zhang, J. Du, H. Wang, J. Guo, J. Zhan, F. Li and F. Yu, *Angew. Chem., Int. Ed.*, 2021, **60**, 24022–24027.
33 J. D. Merline, C. P. Reghunadhan Nair and K. N. Ninan, *J. Macromol. Sci. A*, 2008, **45**, 312–322.
34 D. Huang, H. Zhu, Z. Zhao, J. Huang, P. Liao and X. Chen, *ACS Catal.*, 2022, **12**, 8444–8450.
35 L. Wang, S. Nitopi, A. B. Wong, J. L. Snider, A. C. Nielander, C. G. Morales-Guio, M. Orazov, D. C. Higgins, C. Hahn and T. F. Jaramillo, *Nat. Catal.*, 2019, **2**, 702–708.
36 A. Monshi, M. R. Foroughi and M. R. Monshi, *World J. Nano Sci. Eng.*, 2012, **2**, 154–160.
37 L. Rinawati, R. E. Nugraha, R. M. I. Munifa, U. Chasanah, S. Wahyuningsih and A. H. Ramelan, *J. Chem. Pharm. Res.*, 2015, **7**, 85–89.
38 S. Zhu, T. Li, W. Cai and M. Shao, *ACS Energy Lett.*, 2019, **4**, 682–689.
39 T. Bürgi, *Phys. Chem. Chem. Phys.*, 2001, **3**, 2124–2130.
40 S. Zhu, B. Jiang, W. B. Cai and M. Shao, *J. Am. Chem. Soc.*, 2017, **139**, 15664–15667.
41 Y. Hori, O. Koga, H. Yamazaki and T. Matsuo, *Electrochim. Acta*, 1995, **40**, 2617–2622.
42 J. Zhang, G. Zeng, S. Zhu, H. Tao, Y. Pan, W. Lai, J. Bao, C. Lian, D. Su, M. Shao and H. Huang, *Proc. Natl. Acad. Sci. U. S. A.*, 2023, **120**, e2218987120.
43 Y. Xiao, M. Wang, H. Yang, H. Qiu, H. Lu, Y. Da, G. Chen, T. Jiang, W. Fu, B. Hu, J. Chen, L. Chen, Y. Ding, B. Cui, C. Jiang, Z. Sun, Y. Long, H. Yang, Z. Tian, L. Wang and W. Chen, *Adv. Energy Mater.*, 2024, **14**, 2302556.
44 J. Li, X. Chang, H. Zhang, A. S. Malkani, M. J. Cheng, B. Xu and Q. Lu, *Nat. Commun.*, 2021, **12**, 3264.
45 T. Galimova, M. Ram, D. Bogdanov, M. Fasihi, S. Khalili, A. Gulagi, H. Karjunen, T. N. O. Mensah and C. Breyer, *J. Cleaner Prod.*, 2022, **373**, 133920.
46 C. Breyer, M. Fasihi, C. Bajamundi and F. Creutzig, *Joule*, 2019, **3**, 2053–2057.
47 Z. Xiang, S. Leng and D. Cao, *J. Phys. Chem. C*, 2012, **116**, 10573–10579.
48 X. Nie, M. R. Esopi, M. J. Janik and A. Asthagiri, *Angew. Chem., Int. Ed.*, 2013, **52**, 2459–2462.